Hong Shi
Rentong Zheng
Qianwei Zhang
Jie Yuan
Rui Wang
Mengmeng Cheng
Yitao Zou

http://dx.doi.org/10.21278/brod74401

ISSN 0007-215X
eISSN 1845-5859

Numerical investigation of multi-nozzle ejector device with inclined nozzles for marine gas turbine

UDC 533.697.5:621.438
Original scientific paper

Summary

The high-temperature exhaust gases and the hot surfaces of the ejector device in marine gas turbines generate significant levels of infrared radiation. An appropriate nozzle structure can effectively lower the exhaust gas temperature and reduce the high-temperature radiation surface area, thereby minimizing external infrared radiation. In this study, a numerical simulation of the nozzle structure in the ejector device was conducted using computational fluid dynamics (CFD) methods. By investigating the orthogonal combinations of nozzle inclination angles and the number of nozzles, the temperature distribution and flow characteristics under different operating conditions were analysed. The results showed that as the nozzle inclination angle increased, the entrainment coefficient (C_e) and the temperature ratio at the inlet and outlet (R_t) initially improved but then worsened. Simultaneously, the pressure loss coefficient (C_{pl}) increased with the inclination angle. The CRITIC weight method was employed to objectively allocate weights to R_t, C_e, and C_{pl}, determining the optimal solution. The results indicated that R_t and C_{pl} had significant and similar weights. The optimal solution was found in Case 10 (α = 5°, x = 4), with corresponding evaluation indices of C_e=2.38, C_{pl}=11.45, and =0.68. This study's findings are of great importance for enhancing the performance of marine gas turbines and reducing external infrared radiation.

Key words: ejector; nozzle; CRITIC weight; inclination; marine gas turbine

1. Introduction

Marine gas turbine will produce high temperature exhaust gas when exhausting. In the process of direct exhaust into the environment, it will produce 3 ~ 5 μm band infrared radiation, which is easily detected by infrared detection device [1,2]. The ejector device is used to introduce normal temperature air into the environment to cool the high temperature gas and enable the ship to be infrared stealthy. The ejector device is composed of nozzles, mixing tube, funnels and heat shield. The nozzle discharges high temperature and high

velocity gas, which enters the mixing tube and forms low pressure area inside the mixing tube. Therefore, ambient air enters the mixing tube through the channel between the nozzles and the mixing tube. The high temperature gas in the mixing tube is mixed with the secondary stream to bring reduction of temperature, thereby suppressing infrared radiation.

Exhaust system ejector has done a lot of research in the past few decades. Ellin and Pucci [3] obtained an ejector composed of four straight nozzles in the 1970s, and studied some structural parameters of the ejector. Since then, the research on the structure of the ejector device has been continuously carried out, and various structures of the ejector device have been proposed.

A great deal of studies has focused on nozzle construction. Barik et al [4] conducted a comparative study of device suction when using multiple nozzles of different shapes and suggested that the highest entrainment rates were achieved with five equilateral triangular nozzles when only air entrainment was considered. Wang and Li [5] proposed that when the ratio of mixing tube length to mixing tube diameter is less than 7, the ejection rate of multi-nozzle is higher than that of convergent single nozzle. Chen and Birk [6] studied the effect of nozzle diameter on the pressure and ejection effect of the ejection device. Du and Zhong [7] obtained the conclusion that the aerodynamic performance of four nozzles is better than that of single nozzle through the test and simulation of marine gas turbine exhaust system. Maqsood and Birk [8] studied the curved rectangular ejector device, and concluded that the rectangular nozzle will produce hot spots on the surface of the ejector device, which will adversely affect the ejector device. Ganguly and Dash [9,10] analysed the influence of the number of nozzles at the outlet of the gas turbine. The results showed that the highest entrainment coefficient of the nozzles is achieved when the number of nozzles is 5 or 6. Zare-Behtash et al. [11] studied the nozzles and found that the round nozzles performed better than the elliptic and square nozzles.

In addition to studies on nozzles, there have been many studies on other aspects of gas turbine ejector. Mohanty et al. [12] investigated the flow field of IRS suppression device with a conical funnel and found that cylindrical funnels have higher air entrainment coefficient than conical funnels. Mukherjee et al. [13] proposed a correlation between the mass inlet ratio and temperature ratio of outlet by investigating the geometric parameters of the Infrared Suppression System. Chandrakar et al. [14] researched the comprehensive effect of free convection and surface radiation in infrared suppression devices and showed that surface radiation can influence the convection characteristics. Dash and Barik [15] studied this numerically by examining different parameters of the IRS device. They found that entrainment coefficient into the IRS increases with increasing diameter and the Rayleigh number. For numerical simulation of turbulence models, many papers have chosen the k-ε model after investigating [10,16-18].

The structure of the ejector for marine gas turbines is composed of multiple components, including a mixer, funnel and nozzle, among others. Among them, the nozzle is a key component that can improve the ejection performance. Currently, existing research on ejector mainly focuses on the experimental and numerical simulation of structural parameters for the mixer and funnel, such as the slot height ratio and overlap degree. In contrast, less researches have been done on the nozzles of ejector, and these researches mainly concentrated on the number and shape of the nozzle outlet. The nozzle of the ejector device has a direct impact on changing the flow state of the mainstream fluid in the exhaust tube. In the design of traditional multi-nozzle ejector devices, in order to avoid the collision between the mainstream fluid and the wall of the mixing tube after flowing out of the nozzle, it is necessary to sacrifice some entrainment coefficient or adjust the size of the mixing tube to satisfy the requirements. Therefore, compared with the conventional nozzle, the nozzle

structure studied in this paper has an inclined angle. Considering that the inclination of the nozzle will result in pressure loss, the structure of the inclined nozzle is optimized and its ejection mechanism is simulated using fluid dynamics methods. Furthermore, this paper applies the orthogonal analysis method to study the influence of nozzle inclination angle and number on ejection performance. The CRITIC weight method is used to evaluate all cases to obtain an optimal ejector device structure. The conclusions of this paper contribute to improving the infrared suppression capability of gas turbine exhaust and provide important reference for the optimization design of ejector devices.

2. Numerical simulation

2.1 Problem description

Fig. 1 presents a schematic diagram of the ejector device structure with inclined nozzles. The device consists of nozzles, mixing tube, funnels, and heat shield. As depicted in Fig. 1, the nozzle discharges high-temperature and high-velocity exhaust gases, which enter the mixing tube and create a low-pressure zone. Consequently, ambient air enters the mixing tube through the gap between the nozzle and the mixing tube. The dimensions of the ejector device are based on an actual marine injection device, and detailed parameters can be found in Table 1. The cylindrical computational domain is located outside the injection device. Previous studies by Mukherjee et al. [19] have demonstrated that such a domain size is sufficient to ensure the accuracy of the simulation. The model processing information is provided in Table 2.

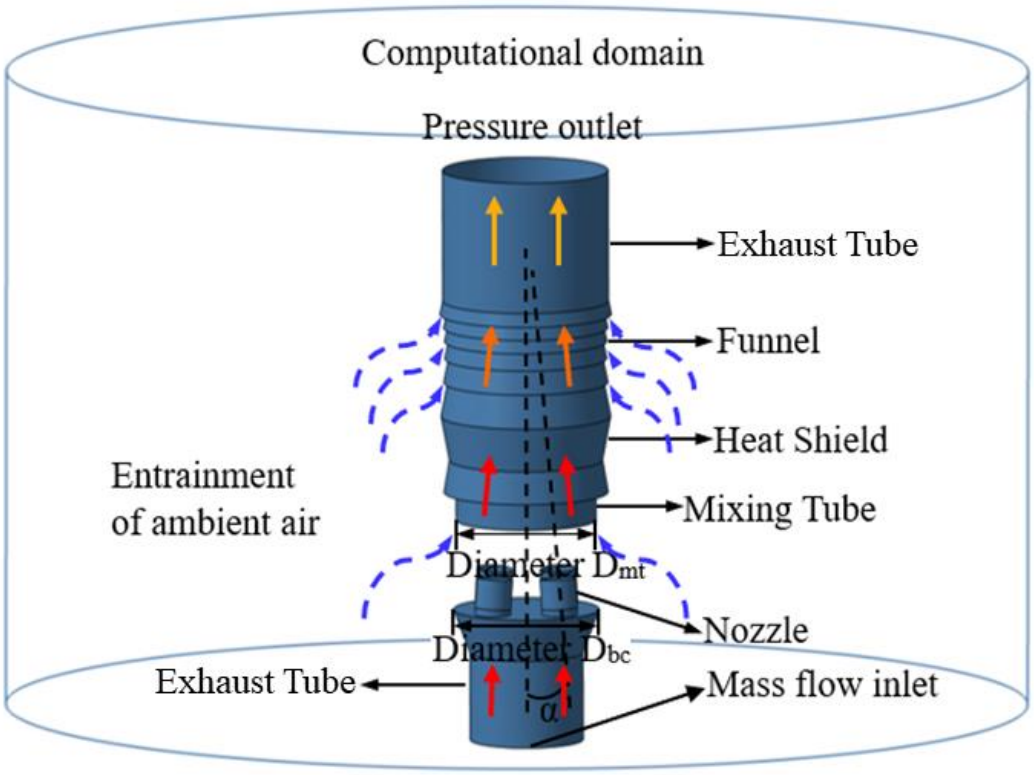

Fig. 1 Structural diagram of the ejector device and computational domain

Table 1 Parameters of ejector dimensions

Parameters				Value
Ejector device	Ejector	Height		10100 mm
	Nozzle	Outlet total area		2010619 mm^2
		Diameter D_n	3 nozzles	923.76 mm
			4 nozzles	800.00 mm
			5 nozzles	715.54 mm
		Diameter of the bottom circular surface D_{bc}		3300 mm
	Mixing tube	Diameter D_{mt}		3200 mm
		Length L_{mt}		3250 mm

Table 2 Model processing information

Processing	Content	Methods
Model	Initial model building	Catia
CFD model	Model simplification	ICEM
	Grid division	ICEM Fluent Meshing
Simulation calculation	Simulation	Fluent
	Solver	Pressure-Based
Post-processing of results	Result export and processing	Tecplot CFD-Post

Table 3 Combination cases

Case	Design Parameters		Case	Design Parameters		Case	Design Parameters	
	Nozzle Inclination Angle(α)	Nozzles number (x)		Nozzle Inclination Angle(α)	Nozzles number (x)		Nozzle Inclination Angle(α)	Nozzles number (x)
1	0	3	8	0	4	15	0	5
2	2.5	3	9	2.5	4	16	2.5	5
3	5	3	10	5	4	17	5	5
4	7.5	3	11	7.5	4	18	7.5	5
5	10	3	12	10	4	19	10	5
6	12.5	3	13	12.5	4	20	12.5	5
7	15	3	14	15	4	21	15	5

The relative distribution of the nozzles is illustrated in Fig. 2. Additionally, orthogonal combinations were performed with seven different nozzle inclination angles (α) and three different nozzle quantities (x), resulting in 21 combinations as shown in Table 3.

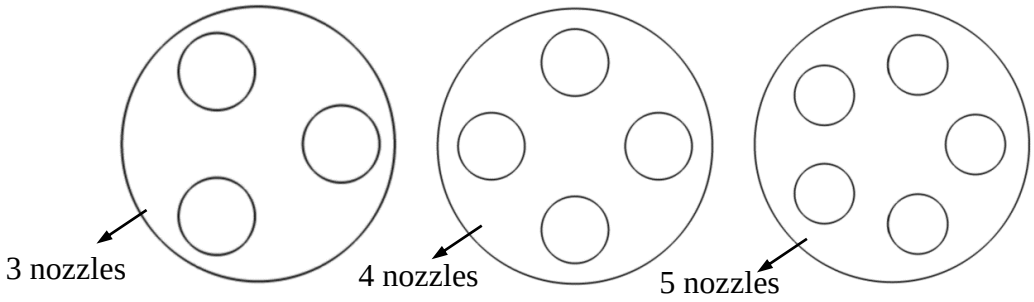

Fig. 2 Top view of ejector with different nozzles number

2.2 Governing equations

The motion and heat transfer of fluid involves the laws of mass conservation, momentum conservation and energy conservation. The equations for a compressible Newtonian fluid are as follows:

Continuity equation:

$$\frac{\partial \rho}{\partial t}+\frac{\partial}{\partial x_i}\left(\rho u_i\right)=0 \tag{1}$$

Momentum equation:

$$\frac{\partial}{\partial t}\left(\rho u_i\right)+\frac{\partial}{\partial x_j}\left(\rho u_i u_j\right)=-\frac{\partial p}{\partial x_i}+\frac{\partial \tau_{ij}}{\partial x_{\mathrm{j}}} \tag{2}$$

For Newtonian fluids there is:

$$\tau_{ij}=\mu\left(\frac{\partial u_i}{\partial x_j}+\frac{\partial u_j}{\partial x_i}\right)-\frac{2}{3}\mu\frac{\partial u_k}{\partial x_k}\delta_{ij} \tag{3}$$

Energy equation:

$$\frac{\partial}{\partial t}\left[\rho\left(e+\frac{1}{2}u_i u_j\right)\right]+\frac{\partial}{\partial x_i}\left\{u_i\left[\rho\left(e+\frac{1}{2}u_i u_j\right)+p\right]\right\}=\frac{\partial}{\partial x_i}\left(k\frac{\partial T}{\partial x_i}+u_j\tau_{ij}\right) \tag{4}$$

Ideal gas equation of state:

$$\frac{P}{\rho}=RT \tag{5}$$

For the non-closure of the RANS equation when using the Reynolds time-averaged simulation method, the Realizable k-ε turbulence model is used to realize the closure. The modelled transport equations for k and ε are as follows:

Turbulent kinetic energy k:

$$\frac{\partial}{\partial t}(\rho k)+\frac{\partial}{\partial x_j}(\rho k u_j)=\frac{\partial}{\partial x_j}[(\mu+\frac{\mu_t}{\sigma_k})\frac{\partial k}{\partial x_j}]+G_k+G_b-\rho\varepsilon-Y_M \tag{6}$$

Turbulent dissipation rate ε:

$$\frac{\partial}{\partial t}(\rho\varepsilon)+\frac{\partial}{\partial x_j}(\rho\varepsilon u_j)=\frac{\partial}{\partial x_j}[(\mu+\frac{\mu_t}{\sigma_\varepsilon})\frac{\partial\varepsilon}{\partial x_j}]+\rho C_1 S\varepsilon-\rho C_2\frac{\varepsilon^2}{k+\sqrt{\nu\varepsilon}}+C_{1\varepsilon}C_{3\varepsilon}C_b \tag{7}$$

where, $C_1=\max\left[0.43,\frac{\eta}{\eta+5}\right]$, $\eta=S\frac{k}{\varepsilon}$, $C_{3\varepsilon}=\tanh\left|\frac{v}{u}\right|$, C_2 = 1.9, $C_{1\varepsilon}$ = 1.44, σ_k = 1.0, σ_ε = 1.2.

2.3 Boundary conditions

The boundary conditions refer to the studies of Gunes [20] and Matulić et al [21] on ship emissions. The airflow characteristics are those of an ideal gas. For each structure of the ejector device is set as no-slip wall surface [22]. The boundary conditions are shown in Fig. 1 and Table 4.

Table 4 Boundary conditions

Part	Conditions	Parameter settings	
Ejector inlet	Mass flow inlet	80 kg/s	773 K
Computational domain outlet	Pressure outlet	Gauge pressure 0 Pa	Back-flow temperature 300 K

2.4 Evaluation indexes

To obtain an optimal ejector device, the entrainment coefficient is not used as the only evaluation index when designing the ejector device under the premise of meeting the cooling requirements [23]. In this paper, entrainment coefficient, pressure loss coefficient and temperature ratio of inlet and outlet are used as evaluation indexes. Entrainment coefficient is a positive index, while pressure loss coefficient and temperature ratio of inlet and outlet are negative indexes.

2.4.1 Entrainment coefficient (C_e)

Entrainment coefficient (C_e) represents the ability of the device to entrain secondary flow fluid, and the larger the C_e, the stronger the air entrainment capacity of the ejector device. The equation is as follows:

$$C_e=\frac{G_2}{G_1} \tag{8}$$

where G_1 is the mainstream fluid mass flow rate. G_2 is the secondary fluid mass flow rate.

2.4.2 Pressure loss coefficient (C_{pl})

Pressure loss coefficient (C_{pl}) is dimensionless. And it represents the flow loss of the whole system. The equation is as follows:

$$C_{pl}=\frac{P_1-P_2}{q} \tag{9}$$

where P_1 represents total pressure at the inlet of the ejector device and P_2 represents total pressure at the outlet of the ejector device. q represents the dynamic pressure at the inlet of the ejector device [24].

2.4.3 Temperature ratio of inlet and outlet (R_t)

Temperature ratio of inlet and outlet (R_t) is the ratio of the highest outlet temperature of the ejector device to the inlet temperature, which represents the cooling capacity of the ejector device. The smaller the R_t, the better the cooling effect of the device. The equation is as follows:

$$R_t = \frac{T_{\max}}{T_1} \tag{10}$$

where T_{max} indicates the maximum temperature at the outlet of ejector device and T_1 indicates the temperature of the mainstream fluid at the inlet.

2.5 Validation of numerical methodology

The ejector device model used in this study is mainly composed of exhaust tube, four equal diameter nozzles, mixing tube and funnels. The experimental device is shown in Fig. 3, and its structure size is as follows in Table 5.

Table 5 Structural dimensions of the experimental setup

Diameter of exhaust tube	Diameter of nozzle	Height of nozzle	Diameter of mixing tube	Height of mixing tube
164 mm	31 mm	50 mm	164 mm	500 mm

A geometric model was created in the Catia software based on the dimensions of the experimental setup model, followed by subsequent numerical simulations. The ejector inlet in the experimental boundary conditions was set as a mass flow inlet of 0.28 kg/s and a temperature of 300 K. The outlet was set up as a pressure outlet with a gauge pressure of 0 Pa and a back-flow temperature of 300 K.

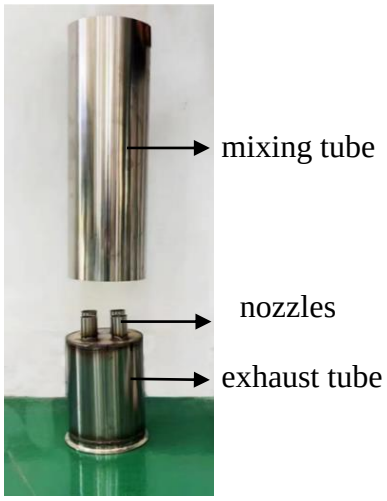

Fig. 3 Experimental model

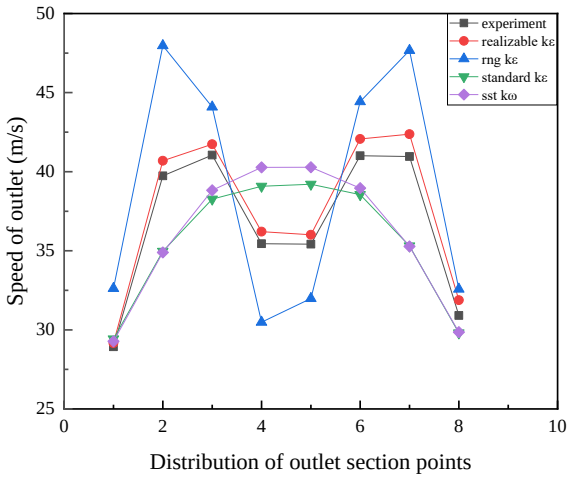

Fig. 4 Comparison of simulation results with experimental results

Fig. 4 shows the velocity distribution at the outlet of mixing tube for the experiment and the numerical simulation for each turbulence model. The velocity distributions of the rng *k*-*ε* model and the realizable *k*-*ε* model are similar to the test results. The velocity distribution of the realizable *k*-*ε* turbulence model is more closely matched to the velocity distribution of the experiment. Therefore, the realizable *k*-*ε* turbulence model predicts the actual parameter

values more accurately than other turbulence models, but overestimates the entrainment coefficient and outlet velocity.

2.6 Mesh independence

Table 6 shows the results of the grid independence test. The geometric model of case8 ($\alpha = 0°$, $x = 4$) was chosen to create five different sizes of meshes. When the number of grids was up to 3.1 million, the entrainment coefficient, pressure loss coefficient and temperature ratio of inlet and outlet of the ejector hardly changed as the number of meshes increased. Considering the accuracy of entrainment coefficient (C_e), pressure loss coefficient (C_{pl}) and temperature ratio of inlet and outlet (R_t), a grid size of 3.1 million was chosen for the numerical simulation. The structural mesh is generated as shown in Fig. 5.

Table 6 Mesh independence validation

Number of meshes	0.9 million	1.9 million	3.1 million	3.9 million	5.1 million
Entrainment coefficient (C_e)	2.121	2.192	2.269	2.271	2.274
Temperature ratio of inlet and outlet (R_t)	0.803	0.779	0.745	0.741	0.739
Pressure loss coefficient (C_{pl})	10.626	10.083	9.891	9.879	9.851

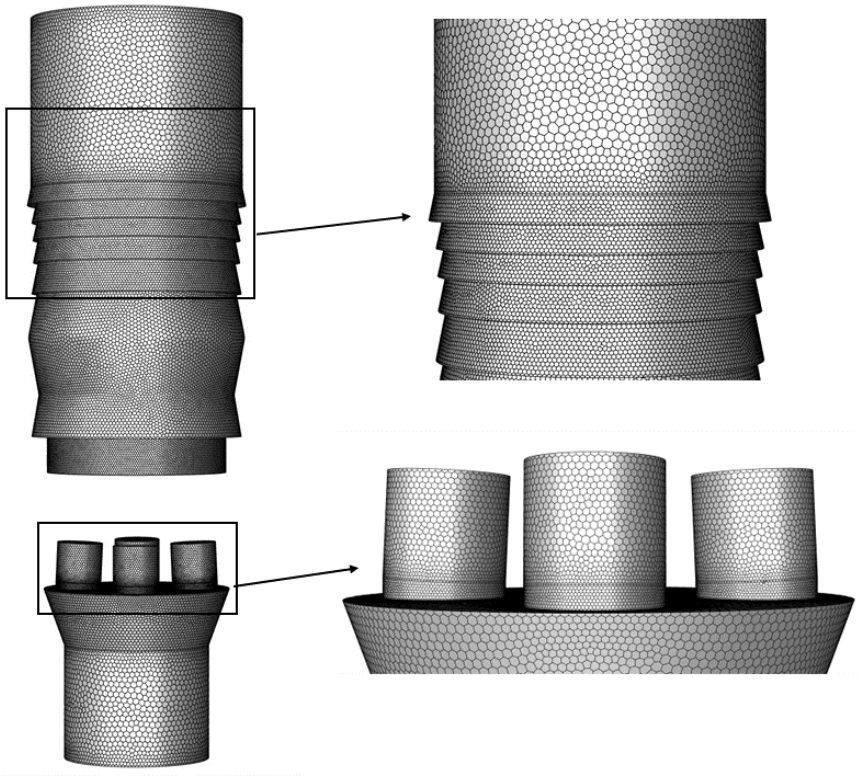

Fig. 5 Schematic of structural mesh

3. Results and discussion

3.1 Entrainment coefficient

Fig. 6 illustrates the variation of the entrainment coefficient (C_e) with the nozzle inclination angle α, as well as the number of nozzles x.

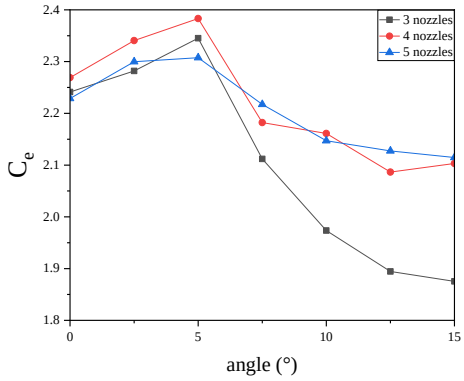

Fig. 6 Variation of entrainment coefficient with angle

According to Fig. 6, the variation trend of the entrainment coefficient under different nozzle inclinations and nozzle quantities is primarily characterized by an initial increase followed by a decrease. As the nozzle inclination angle α increases, the entrainment coefficient gradually increases until $\alpha \leq 5°$. Conversely, when $\alpha \geq 5°$, the entrainment coefficient gradually decreases.

To further investigate the influence mechanism of the nozzle inclination angle α on the entrainment coefficient, a specific analysis is conducted using a schematic diagram of velocity vector with nozzle quantity $x = 4$. The location of the typical plane is illustrated in Fig. 7. Fig. 8 presents the schematic diagrams of velocity vector on the typical plane for nozzle inclination angles $\alpha = 0°$, 2.5°, 5°, 7.5°, and 10°, respectively. Furthermore, Fig. 9 reveals the variation of the volume proportion of fluids with velocity above 30 m/s on the inlet plane of the mixing tube for different nozzle inclination angles α. Fig. 10 shows the variation of the maximum velocity on the inlet plane of the mixing tube with angle.

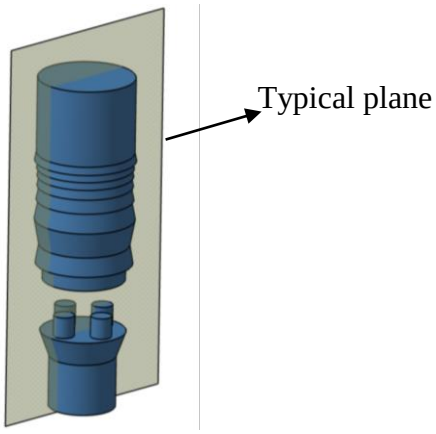

Fig. 7 Schematic of the location of the typical plane

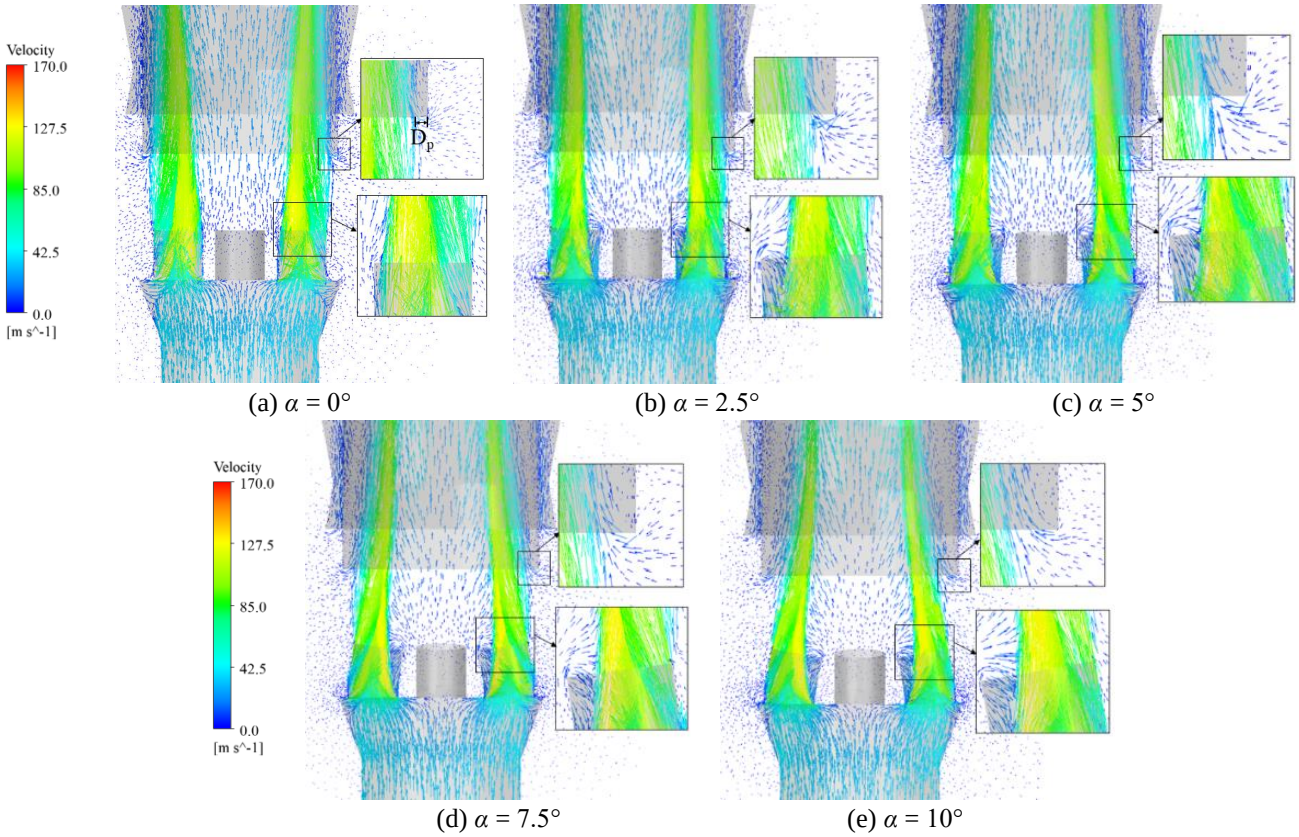

(a) α = 0° (b) α = 2.5° (c) α = 5°

(d) α = 7.5° (e) α = 10°

Fig. 8 Velocity vector on the typical plane

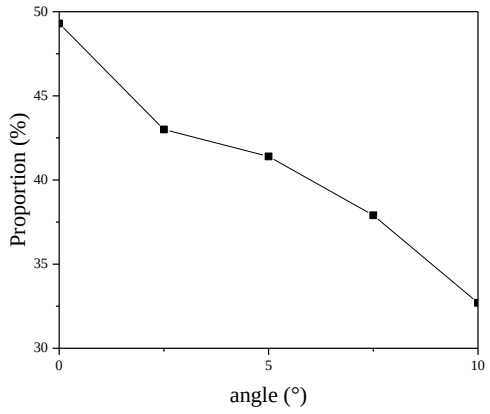

Fig. 9 Variation of the proportion of fluids with velocities above 30 m/s with angle

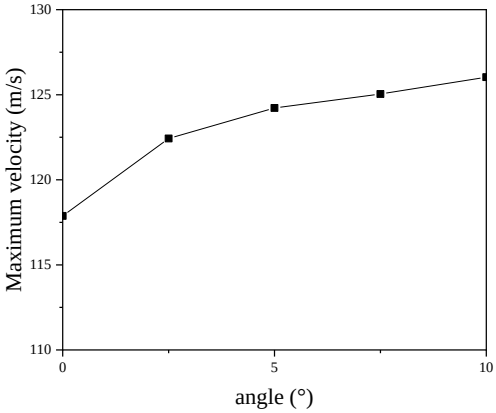

Fig. 10 Variation of the maximum velocity on the inlet plane of the mixing tube with angle

According to Fig. 8, when the inclination angle α is less than 5°, an increase in the nozzle inclination angle causes the mainstream fluid to converge towards the center axis of the device, resulting in an increasing distance (D_p) between the mainstream fluid and the mixing tube wall. This convergence facilitates the entry of more air into the mixing tube, thereby increasing the entrainment coefficient. However, due to the inclined nozzle, the contact area between the converged mainstream fluid and the surrounding cold air decreases, which hinders the enhancement of the entrainment coefficient. Specifically, as the mainstream fluid converges towards the center axis of the device, the volume proportion of fluid with a velocity exceeding 30 m/s noticeably decreases (refer to Fig. 9). When the inclination angle α is greater than or equal to 5°, this ultimately leads to a decrease in the entrainment coefficient. It is worth noting that Fig. 10 illustrates that with an increasing inclination angle, the streamline of the mainstream fluid becomes more converged. However, due to the inertia of the fluid, the effective throat area of the flow decreases, resulting in an increase in local fluid velocity. Nevertheless, the improvement in entrainment coefficient resulting from this velocity increase is minimal. Therefore, the entrainment coefficient exhibits an increasing trend followed by a decreasing trend due to the combined effects of changes in the cold air flow area, the contact area between high-speed and low-speed fluids, and the velocity of the mainstream fluid.

3.2 Pressure loss coefficient

Fig. 11 shows the pressure loss coefficient (C_{pl}) variation with different nozzle inclination angle α and the number of nozzles x.

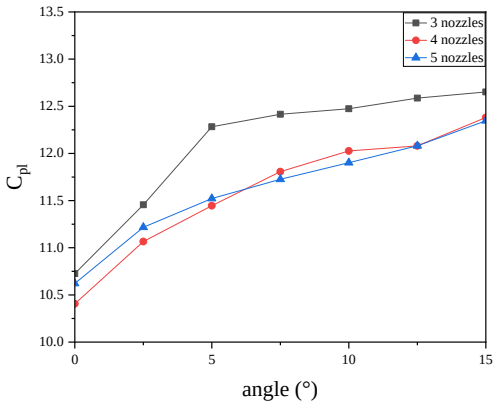

Fig. 11 Variation of pressure loss coefficient with angle

As shown in Fig. 11, with an increasing nozzle inclination angle α and for nozzle quantities x = 3, 4, and 5, the pressure loss coefficient gradually increases due to the enhanced local resistance at the nozzle. Additionally, in conjunction with Fig. 8, when the nozzle is inclined, the mainstream flow tends to concentrate towards one side of the nozzle, resulting in a reverse flow phenomenon on the other side, which obstructs the flow and leads to an increased pressure loss.

3.3 Temperature ratio of inlet and outlet

Fig. 12 illustrates the variation of the temperature ratio between the inlet and outlet (R_t) with different nozzle inclination angles α and nozzle quantities x. Fig. 13 presents schematic diagrams of the temperature distribution on the outlet plane for nozzle inclination angles α = 0°, 2.5°, 5°, 7.5°, and 10°.

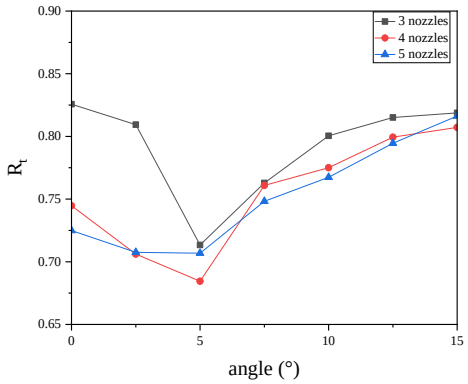

Fig. 12 Variation of temperature ratio of inlet and outlet with angle

According to Fig. 12, the variation trend of the inlet-to-outlet temperature ratio (R_t) is characterized by a decrease followed by an increase when considering different nozzle inclination angles (α) and nozzle quantities (x). Specifically, as the nozzle inclination angle (α) increases, R_t decreases when $\alpha \leq 5°$, while R_t increases when $\alpha \geq 5°$.

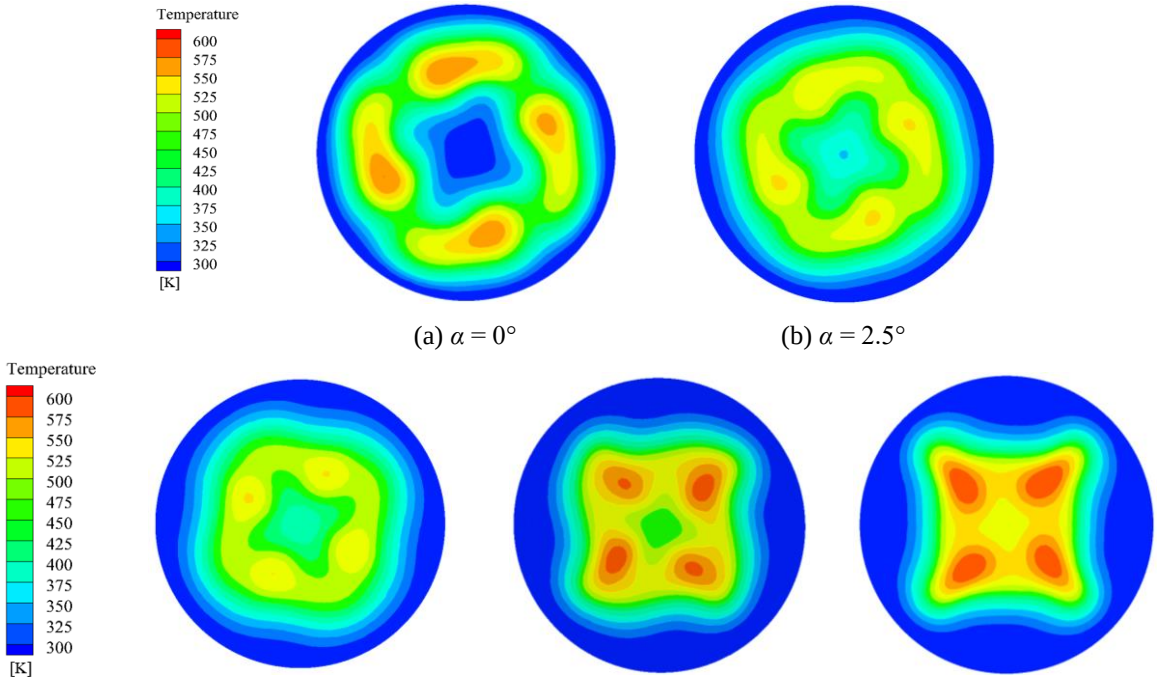

(a) $\alpha = 0°$ (b) $\alpha = 2.5°$

(c) $\alpha = 5°$ (d) $\alpha = 7.5°$ (e) $\alpha = 10°$

Fig. 13 Temperature distribution on the outlet plane (x = 4)

Furthermore, Fig. 13 reveals that a slight inclination angle of the nozzle favors the mixing degree of the fluid within the mixing tube. A smaller inclination angle leads to a more dispersed distribution of high-temperature regions in the outlet plane, indicating a higher degree of mixing. Conversely, a larger inclination angle concentrates the high-temperature regions, resulting in a poorer mixing performance.

By considering the variation of the entrainment coefficient depicted in Fig. 6, it can be deduced that the minimum inlet-to-outlet temperature ratio and thus the optimal cooling effect are achieved when the nozzle inclination angle is 5°.

3.4 Comprehensive evaluation

3.4.1 CRITIC weight method

The CRITIC weight method is a comprehensive measure of objective weights for evaluation indexes based on the comparative intensity and conflict between indexes. Comparative intensity is the size of the difference in values of the same indicator in various evaluation situations and is shown in the form of standard deviation. The larger the standard deviation, the higher the weight. Conflicts between indicators are expressed as correlation coefficients. If two indexes have a strong positive correlation, their conflict is smaller and the weight is lower. CRITIC weight method is partially calculated by referring to the study of Liu et al. [25].

3.4.2 Results

The CRITIC weight method was applied to evaluate the comprehensive performance of 21 cases based on three indicators: entrainment coefficient, pressure loss coefficient and temperature ratio of inlet and outlet. The results are shown in Table 7.

Table 7 Results of CRITIC weight

Index	Index variability	Index conflict	Information content	Weight
C_e	0.277	0.565	0.156	23.51%
R_t	0.298	0.854	0.254	38.21%
C_{pl}	0.319	0.799	0.255	38.28%

According to Table 7, it can be seen that the weight of the R_t and the C_{pl} is relatively large and close, which has a significant impact on the overall evaluation.

Based on the weight of each evaluation index, further analysis was conducted on the 21 cases to find the optimal structural parameters. The specific optimization results are in Table 8.

Table 8 Optimization results

case	CompScore	case	CompScore	case	CompScore
1	0.497	8	0.784	15	0.782
2	0.436	9	0.809	16	0.761
3	0.585	10	0.823	17	0.715
4	0.320	11	0.461	18	0.526
5	0.144	12	0.376	19	0.412
6	0.049	13	0.266	20	0.298
7	0.019	14	0.202	21	0.189

It can be seen from Table 8 that case 10 (α = 5°, x = 4) has the highest comprehensive score, with C_e = 2.38, C_{pl} = 11.45 and R_t =0.68. The final optimization results show that compared with the nozzle with inclination angle of α = 0°, the optimal case sacrifices some pressure loss coefficient, greatly improving the entrainment coefficient and cooling effect.

4. Conclusion

The nozzle structure of the ejector device was optimized in this study, taking into consideration the entrainment coefficient, pressure loss coefficient, and inlet/outlet temperature ratio. By incorporating suitable nozzle angles and nozzle quantities, the nozzle structure was proposed. Numerical simulations of the ejector device were performed, and the temperature distribution and flow characteristics under different operating conditions were analysed through orthogonal combinations of nozzle angles and nozzle quantities. The conclusions are as follows:

(1) For the ejector device with inclined nozzles, as the nozzle angle increases, the space of the air into the mixing tube grows larger, resulting in an increase in the entrainment coefficient. However, compared to the fluid at the lower angle, the mainstream fluid flowing out of the nozzle becomes more concentrated with the increasing nozzle inclination angle, which decreases the proportion of the volume of the fluid with high velocity, leading to a decrease in the contact area of high-velocity fluid with the air, which hinders the enhancement of the entrainment coefficient. It is worth noting that as the inclination angle increases, there is a slight increase in the local fluid velocity. Nevertheless, the improvement in entrainment coefficient resulting from this velocity increase is minimal. Therefore, the entrainment coefficient exhibits an increasing-decreasing trend with increasing nozzle angles.

(2) As the nozzle angles increase, the nozzle experiences higher local resistance. Additionally, the occurrence of secondary flow reversal within the nozzle obstructs the flow of the mainstream fluid to some extent. Consequently, the pressure loss coefficient gradually rises as the nozzle angles become larger.

(3) Slight nozzle inclination is beneficial for fluid mixing. However, considering the influence of the entrainment coefficient and the degree of temperature mixing inside the mixing tube on the inlet/outlet temperature ratio, the inlet/outlet temperature ratio demonstrates a decreasing-increasing trend with increasing nozzle angles.

(4) By utilizing the CRITIC weighting method, a comprehensive evaluation of 21 cases is conducted, with weights assigned to C_e, C_{pl}, and R_t as 23.51%, 38.21%, and 38.28%, respectively. Based on the weight coefficients, the optimal operating condition is identified as Case 10 (α=5°, x=4), corresponding to evaluation parameters C_e=2.38, C_{pl}=11.45, and R_t=0.68.

REFERENCES

[1] Birk, A. M., Davis, W. R., 1989. Suppressing the Infrared Signatures of Marine Gas Turbines. *Journal of Engineering for Gas Turbines and Power*, 111(1), 123-129. https://doi.org/10.1115/1.3240210

[2] Pašagić, V., Mužević, M., Kelenc, D., 2008. Infrared Thermography in Marine Applications. *Brodogradnja*, 59(2), 123-130.

[3] Ellin, C. R., Pucci, P. F., 1977. Model Tests of Multiple Nozzle Exhaust Gas Eductor Systems for Gas Turbine Powered Ships. *Naval Postgraduate School*.

[4] Barik, A. K., Dash, S. K., Guha A., 2015. Entrainment of Air into an Infrared Suppression (IRS) Device Using Circular and Non-circular Multiple Nozzles. *Computers & Fluids*, 114, 26-38. https://doi.org/10.1016/j.compfluid.2015.02.016

[5] Wang, S. F., Li, L. G., 1996. Performance Analysis of Multi-nozzle Ejector. *Journal of Nanjing University of Aeronautics and Astronautics*, 3, 52-58.

[6] Chen, Q., Birk, A. M., 2009. Experimental Study of Oblong Exhaust Ejectors with Multiring Oblong Entraining Diffusers. *Journal of Engineering for Gas Turbines and Power*, 131(6), 062302. https://doi.org/10.1115/1.2943195

[7] Du, C. H., Zhong, F. Y., 1995. Flow Analysis of Exhaust Infrared Suppression Devices for Marine Gas Turbine. *Ship Engineering*, 6, 25-28+2.

[8] Maqsood, A., Birk, A. M., 2017. Wall Pressure and Temperature Distribution in Bent Oblong Exhaust Ejectors. *Turbo Expo: Turbomachinery Technical Conference and Exposition*, 50794. https://doi.org/10.1115/GT2017-63250

[9] Ganguly, V. R., Dash, S. K., 2020. Numerical analysis of air entrainment and exit temperature of a real scale conical infrared suppression (IRS) device. *International Journal of Thermal Sciences*, 156, 106482. https://doi.org/10.1016/j.ijthermalsci.2020.106482

[10] Ganguly, V. R., Dash, S. K., 2022. Comparison between a Conventional and a New IRS Device in Terms of Air Entrainment: An Experimental and Numerical Analysis. *Journal of Ship Research*, 64(4), 357–371. https://doi.org/10.5957/JOSR.06190034

[11] Zare-Behtash, H., Gongora-Orozco, N., Kontis, K., 2011. Effect of primary jet geometry on ejector performance: A cold-flow investigation. *International Journal of Heat and Fluid Flow*, 32(3), 596-607. https://doi.org/10.1016/j.ijheatfluidflow.2011.02.013

[12] Mohanty, A., Senapati, S. K., Dash, S. K., 2020. Natural convection cooling of an infrared suppression device (IRS) with conical funnels- a computational approach. *International Communications in Heat and Mass Transfer*, 118, 1-13. https://doi.org/10.1016/j.icheatmasstransfer.2020.104891

[13] Mukherjee, A., Chandrakar, V., Senapati, J. R., 2021, New Correlations for Flow and Conjugate Heat Transfer With Surface Radiation Characteristics of a Real-Scale Infrared Suppression System With Conical Funnels. *Journal of Heat Transfer: transactions of The Asme*, 143(8). https://doi.org/10.1115/1.4051129

[14] Chandrakar, V., Mukherjee, A., Senapati, J. R., Mohanty, A., 2022. Conjugate free convection with surface radiation from real-scale IRS system with multiple conical funnels: A numerical analysis. *International Communications in Heat and Mass Transfer*, 134, 106004. https://doi.org/10.1016/j.icheatmasstransfer.2022.106004

[15] Dash, M. K., Barik, A. K., 2023. A computational study on air-entrainment and pressure distribution for natural convection cooling of a hybrid IRS device. *International Journal of Thermal Sciences*, 187, 108196. https://doi.org/10.1016/j.ijthermalsci.2023.108196

[16] Ganguly, V. R., Dash, S. K., 2019. Experimental and numerical study of air entrainment into a louvered conical IRS device and comparison with existing IRS devices. *International Journal of Thermal Sciences*, 141, 114-132. https://doi.org/10.1016/j.ijthermalsci.2019.03.034

[17] Sahu, S. R., Mishra, D. P., 2017. Maximum air suction into horizontal open ended cylindrical louvered pipe. *Journal of Engineering Science and Technology*, 12(2), 388-404.

[18] Sahu, S. R., Mishra, D. P., 2016. Numerical investigation of maximum air entrainment into cylindrical louvered pipe. *International Journal of Automotive and Mechanical Engineering*, 13(2), 3278-3292. https://doi.org/10.15282/ijame.13.2.2016.1.0273

[19] Mukherjee, A., Chandrakar, V., Senapati, J.R., 2021. Flow and conjugate heat transfer with surface radiation characteristics of a real-scale infrared suppression device with conical funnels. *International Communications in Heat and Mass Transfer*, 123, 105208. https://doi.org/10.1016/j.icheatmasstransfer.2021.105208

[20] Gunes, U., 2023. Estimating bulk carriers' main engine power and emissions. *Brodogradnja*, 74(1), 85-98. https://doi.org/10.21278/brod74105

[21] Matulić, N., Račić, N., Radica, G., 2017. Supercharged engine using turbine standalone exhaust gas recuperation system. *Brodogradnja*, 68(3), 103-118. https://doi.org/10.21278/brod68307

[22] Zou, Y. T., Shi, H., Kong, B. B., Pan, J. S., Jiang, Y. L., 2023. Numerical investigation of air entrainment and wall temperature of a real-scale infrared suppression device with slots of gradient height. *International Journal of Thermal Sciences*, 190, 108296. https://doi.org/10.1016/j.ijthermalsci.2023.108296

[23] Han, Y. L., 2005. Numerical Simulation and Experimental Study of Marine Gas Turbine Exhaust Ejector. *Harbin Engineering University*. https://doi.org/10.7666/d.y780039

[24] Shi, H., Zhang, Q. W., Liu, M. N., Yang, K. J., 2022. Numerical Study of the Ejection Cooling Mechanism of Ventilation for a Marine Gas Turbine Enclosure. *Polish Maritime Research*, 29(3), 119-127. https://doi.org/10.2478/pomr-2022-0032

[25] Liu, Y., Du, J., Li, J. C., Yang, X., Zhu, J. Q., Nie, C. Q., 2023. A stall diagnosis method based on entropy feature identification in axial compressors. *International Journal of Mechanical System Dynamics*, 3(1), 73-84. https://doi.org/10.1002/msd2.12064

Submitted: 26.05.2023.
Accepted: 20.07.2023.

Hong Shi*, shihong@nuaa.edu.cn
College of Energy & Power Engineering, Jiangsu University of Science and Technology, Zhenjiang 212114, China

Rentong Zheng, zhengrt99@163.com
College of Energy & Power Engineering, Jiangsu University of Science and Technology, Zhenjiang 212114, China

Qianwei Zhang, zqw1054200681@163.com
College of Energy & Power Engineering, Jiangsu University of Science and Technology, Zhenjiang 212114, China

Jie Yuan, jieyuan@nuaa.edu.cn
Key Laboratory of Aircraft environment control and life support, MIIT, Nanjing University of Aeronautics & Astronautics, Nanjing 210016, China

Rui Wang, ray980801@outlook.com
College of Energy & Power Engineering, Jiangsu University of Science and Technology, Zhenjiang 212114, China

Mengmeng Cheng, c205552679@163.com
College of Energy & Power Engineering, Jiangsu University of Science and Technology, Zhenjiang 212114, China

Yitao Zou, zouyitao_xl@nuaa.edu.cn
Key Laboratory of Aircraft environment control and life support, MIIT, Nanjing University of Aeronautics & Astronautics, Nanjing 210016, China